The Astronomical Journal, 166:204 (12pp), 2023 November https://doi.org/10.3847/1538-3881/acff72

New Insights on 30 Dor B Revealed by High-quality Multiwavelength Observations

Wei-An Chen (陳韋安)[1,2], Chuan-Jui Li (李傳睿)[2], You-Hua Chu (朱有花)[2], Shutaro Ueda (上田周太朗)[2], Kuo-Song Wang (王國松)[2], Sheng-Yuan Liu (呂聖元)[2], and Bo-An Chen (陳柏安)[3]
[1] Graduate Institute of Astrophysics, National Taiwan University, No. 1, Sec. 4, Roosevelt Rd., Taipei 10617, Taiwan, R.O.C.
[2] Institute of Astronomy and Astrophysics, Academia Sinica, No. 1, Sec. 4, Roosevelt Rd., Taipei 10617, Taiwan, R.O.C.
[3] Department of Physics, National Taiwan University, No. 1, Sec. 4, Roosevelt Rd., Taipei 10617, Taiwan, R.O.C.
Received 2023 July 31; revised 2023 September 22; accepted 2023 September 22; published 2023 October 20

Abstract

The supernova remnant (SNR) 30 Dor B is associated with the H II region ionized by the OB association LH99. The complex interstellar environment has made it difficult to study the physical structure of this SNR. We have used Hubble Space Telescope Hα images to identify SNR shocks and deep Chandra X-ray observations to detect faint diffuse emission. We find that 30 Dor B hosts three zones with very different X-ray surface brightnesses and nebular kinematics that are characteristic of SNRs in different interstellar environments and/or evolutionary stages. The ASKAP 888 MHz map of 30 Dor B shows counterparts to all X-ray emission features except the faint halo. The ASKAP 888 and 1420 MHz observations are used to produce a spectral index map, but its interpretation is complicated by the background thermal emission and the pulsar PSR J0537−6910's flat spectral index. The stellar population in the vicinity of 30 Dor B indicates a continuous star formation in the past 8–10 Myr. The observed very massive stars in LH99 cannot be coeval with the progenitor of 30 Dor B's pulsar. Adopting the pulsar's spin-down timescale, 5000 yr, as the age of the SNR, the X-ray shell would be expanding at ∼4000 km s^{-1} and the post-shock temperature would be 1–2 orders of magnitude higher than that indicated by the X-ray spectra. Thus, the bright central region of 30 Dor B and the X-ray shell requires two separate SN events, and the faint diffuse X-ray halo perhaps other older SN events.

Unified Astronomy Thesaurus concepts: Interstellar medium (847); Supernova remnants (1667); Magellanic Clouds (990); Large Magellanic Cloud (903)

1. Introduction

The name "30 Dor B" originates from the first 408 MHz map that resolved the 30 Doradus (30 Dor) region into A, B, and C components (Le Marne 1968), corresponding to the giant H II region centered on the OB association LH100 (aka the R136 cluster), the H II region of the OB association LH99, and the superbubble around the OB association LH90, respectively (Lucke & Hodge 1970). These three components not only are spatially distinct but also have different stellar population and nebular morphology. The A component has been simply called 30 Dor, while the other two components are commonly called 30 Dor B and 30 Dor C. The high radio-to-optical emission ratio of 30 Dor B led to the suggestion of a supernova remnant (SNR), and its flat radio spectrum prompted the speculation that the SNR might be Crab-like (Mills et al. 1978). The detection of diffuse X-ray emission confirmed the existence of an SNR in 30 Dor B (Long et al. 1981). Strictly speaking, the name "30 Dor B" refers to the region that contains both the H II region of LH99 and the SNR, while the SNR per se should be called MCSNR J0537−6910; however, to keep the name short, we will continue calling the SNR "30 Dor B" in this paper. As 30 Dor has been cataloged as LHA 120-N157 (Henize 1956), or N157 for short, 30 Dor B has also been called N157B.

The position coincidence of 30 Dor B and the H II region photoionized by the OB association LH99 (Lucke & Hodge 1970) points to a probable physical association; thus, its SN progenitor is suggested to be a massive member of LH99 (Chu 1997). 30 Dor B has been observed in essentially all wave bands. Its radio observations made with the Australia Telescope Compact Array at wavelengths of 3.5 and 6 cm indicate a radio spectral index of −0.19 in the pulsar wind nebula (PWN), named PWN N157B (Lazendic et al. 2000). Spitzer IR observations of 30 Dor B reveal mostly thermal emission from dust heated by radiation of massive stars in LH99 (Micelotta et al. 2009). High-dispersion optical spectroscopic observations of 30 Dor B have been used to kinematically identify SNR shocks and boundary (Chu et al. 1992). Rossi X-Ray Timing Explorer observations detected the 16 ms pulsed X-ray emission from the pulsar PSR J0537−6910 (Marshall et al. 1998), and Chandra X-ray observations resolved its PWN (Wang et al. 2001). Even high-energy gamma rays have been detected from this PWN in 30 Dor B (HESS Collaboration et al. 2012).

While 30 Dor B is distinct from the main body of the 30 Dor giant H II region, it has been included in the Hubble Tarantula Treasury Project (HTTP, PI: E. Sabbi) and high-resolution Hubble Space Telescope (HST) continuum and Hα images of 30 Dor B become available in the archive. These images clearly reveal sharp filaments associated with the SNR shocks. 30 Dor B is also included in the Chandra X-ray Observatory's very large program The Tarantula—Revealed by X-rays (T-Rex, PI: L. Townsley), which has mapped 30 Dor with ACIS-I in 2 Ms. This deep observation reveals the full extent of diffuse X-ray emission associated with 30 Dor B and clearly shows, in addition to the PWN, a shell structure and a faint halo. Now is thus an opportune time to reexamine 30 Dor B and make a comprehensive multiwavelength analysis of its structure and relationship with the ambient interstellar medium (ISM). We have retrieved high-resolution multiwavelength images available in archives, evaluated the effectiveness of the SNR

diagnostics, and assessed the physical structure of the 30 Dor B SNR. This paper reports our analysis and results.

2. Observations

We use archival HST mosaic images of 30 Dor from the HTTP (Sabbi et al. 2013, 2016; Sabbi 2016) to study the 30 Dor B SNR and its interactions with the ambient ISM. The HTTP is a panchromatic imaging survey of stellar populations in the Tarantula Nebula (aka 30 Dor). The HST mosaic images used observations made with the Wide Field Channel of the Advanced Camera for Surveys (ACS/WFC), the UVIS channel of the Wide Field Camera 3 (WFC3/UVIS), and the IR channel of the Wide Field Camera 3 (WFC3/IR) from mainly Program 12939 (PI: E. Sabbi) and partly Program 12499 (PI: D. Lennon). For these mosaic images, the pixel size is 0.″04, corresponding to 0.01 pc in the Large Magellanic Cloud (LMC, at a distance of 50 kpc), and the orientation (the up direction) is 35° clockwise from the north. The available HST mosaic images from the HTTP are listed in Table 1. The HTTP data product described above may be retrieved from the MAST archive (Sabbi 2016).

The Magellanic Cloud Emission Line Survey (MCELS) has provided Hα λ6563, [O III] λ5007, and [S II] $\lambda\lambda$6716, 6731 line images, as well as red continuum ($\lambda_c = 6850$ Å, $\Delta\lambda = 95$ Å) and green continuum ($\lambda_c = 5130$ Å, $\Delta\lambda = 155$ Å) images at a $\sim$2″ resolution (Smith & MCELS Team 1999). These images have been used to produce continuum-subtracted, flux-calibrated line images. For higher-resolution line images, we have also used Hα, [S II], and [O III] images taken with the MOSAIC camera on the Blanco 4 m Telescope at Cerro Tololo Inter-American Observatory (CTIO). The image pixel size is 0.″27, and the seeing measured from the FWHM of stellar image profiles is $\sim$1″. We have carried out a crude flux calibration for nebular emission in the 4 m MOSAIC Hα and [S II] images by scaling from the flux-calibrated MCELS images. Ten regions of different surface brightnesses without significant star emission were selected from the Hα and [S II] images, and the scaling is based on linear regressions between the MCELS fluxes and the MOSAIC counts. These flux-calibrated MOSAIC images will be used mainly to search for [S II]/Hα enhancements in 30 Dor B.

In addition to optical images, high-dispersion echelle spectra of the Hα + [N II] and [S II] lines reported by Chu et al. (1992) are reexamined for correlations between high-velocity shocked gas and diffuse X-ray emission detected in the 2 Ms Chandra observation.

In the Chandra archive, we have found 59 data sets from Advanced CCD Imaging Spectrometer (ACIS; Garmire et al. 2003) observations of 30 Dor, including the 2 Ms observations from the T-Rex program and the earlier short exposures. Only one data set was obtained with the ACIS-S, and the rest were obtained with ACIS-I. These Chandra data sets, obtained by the Chandra X-ray Observatory, can be retrieved from DOI:10.25574/cdc.156. The Chandra Interactive Analysis of Observations (CIAO; Fruscione et al. 2006) version 4.15 and the Calibration Database (CALDB) version 4.10.2 were used to process the data, remove the periods of background flares, and produce a 2.18 Ms Chandra X-ray image in the 0.5–7.0 keV band for this paper. The image has a pixel size of 0.″5 and a resolution of $\sim$1″. The details of reduction and analysis of the Chandra X-ray observations will be reported in a separate paper (S. Ueda et al. 2023, in preparation).

The Australian Square Kilometre Array Pathfinder (ASKAP) has mapped the LMC at 888 MHz with a beam size of 13.″9 × 12.″1 and a bandwidth of 288 MHz (Project AS033; Pennock et al. 2021) and at 1420 MHz with a beam size of 9.″6 ×7.″3 and a bandwidth of 288 MHz (Project AS108). These high-resolution maps were used to derive spectral index and compared with the X-ray image to assess the effectiveness of three canonical SNR diagnostics, namely, diffuse X-ray emission, nonthermal radio spectral index, and high [S II]/Hα ratios.

Table 1
HST Observations

Program ID	PI	Instrument	Filter
GO-12499	D. Lennon	ACS/WFC	F775W
.	.	WFC3/UVIS	F775W
GO-12939	E. Sabbi	ACS/WFC	F555W
.	.	ACS/WFC	F658N
.	.	WFC3/IR	F110W
.	.	WFC3/IR	F160W
.	.	WFC3/UVIS	F275W
.	.	WFC3/UVIS	F336W

Note. See Sabbi et al. (2013, 2016) for further details about the observations.

For completeness, we have also examined the Spitzer Space Telescope images of 30 Dor B, particularly the IRAC 8 μm image that shows polycyclic aromatic hydrocarbon (PAH) emission from the partially dissociated regions and the MIPS 24 μm image that shows thermal dust emission. These data are from the Spitzer survey of the LMC (PI: M. Meixner; Meixner et al. 2006). The resolution of the IRAC 8 μm image is $\sim$2″, and that of the MIPS 24 μm image is $\sim$6″.

The above multiwavelength images are shown in Figure 1, which includes the 4 m MOSAIC images in Hα, [S II], and [O III] lines; HST Hα image; 4 m MOSAIC [S II]/Hα ratio map; Chandra X-ray image in the 0.5–7.0 keV energy band; ASKAP 888 MHz map; and Spitzer 8 and 24 μm images.

Finally, for the stellar content of LH99 we use the photometry and spectroscopic classifications from the VLT-FLAMES Tarantula Survey (Evans et al. 2011; Schneider et al. 2018). This survey, like the HTTP program, includes both the 30 Dor giant H II region and the 30 Dor B region.

3. Multiwavelength View of 30 Dor B

Figure 1 shows multiwavelength images of 30 Dor B. While evolved SNRs usually show shell structures in optical emission lines, 30 Dor B does not exhibit any shell structure in the 4 m MOSAIC images in Hα, [S II], and [O III] lines. The Hα and [S II] images are qualitatively similar, and the [O III] image appears more amorphous. The narrow filaments in Hα and [S II] images become much less conspicuous in the [O III] line.

The HST Hα image clearly resolves sharp filaments associated with SNR shocks that are not discernible in ground-based images. Figure 2 shows a close-up of the HST Hα image of 30 Dor B and the same image with visually identified filaments marked. Long filamentary arcs are present, but still no coherent shell structure can be recognized in the HST Hα image.

The Chandra X-ray image in the 0.5–7.0 keV band extracted from 2.18 Ms observations shows not only the bright PWN but also a large shell structure about 2.′6 ($\sim$40 pc) in diameter. The PWN is off-center toward the south edge of the shell structure. The extended diffuse X-ray emission has no obvious optical counterpart, and the X-ray shell extends well beyond the bright photoionized region of 30 Dor B. Outside the X-ray shell, a

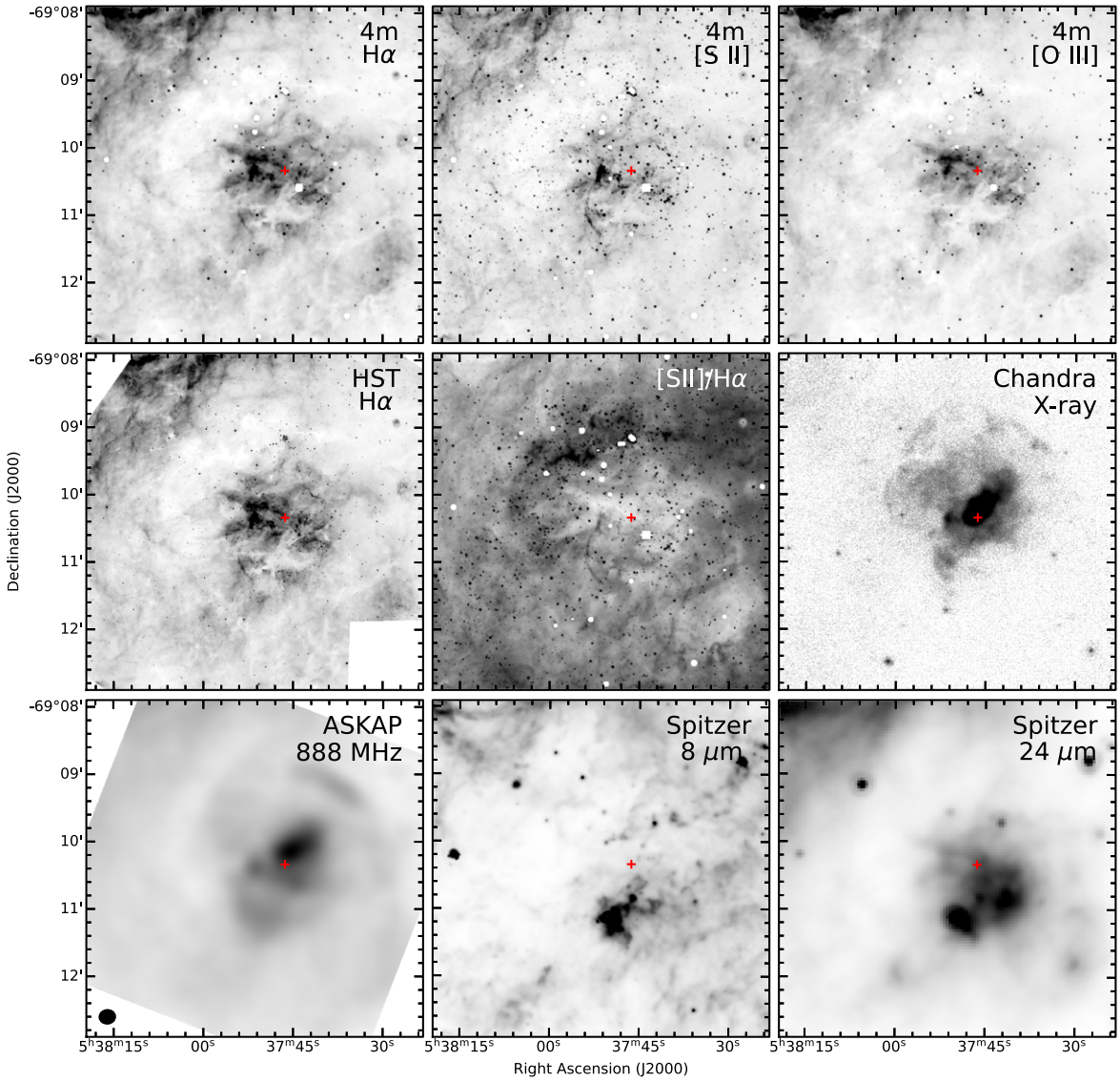

Figure 1. Multiband images of 30 Dor B. All images use an "inverted colormap" with high values in black and low values in white. The top row shows the Hα, [S II], and [O III] images taken with the MOSAIC camera on the Blanco 4 m telescope. The white spots are bright stars that are saturated in the MOSAIC images. The middle row shows the Hα image from HST, [S II]/Hα ratio from 4 m MOSAIC images (see Figure 8 for ratio maps with color bar), and X-ray 0.5–7.0 keV band image (log scale) from 2.18 Ms Chandra ACIS observations. The bottom row shows the radio image at 888 MHz from ASKAP (square root scale, with the beam plotted in the lower left corner) and IRAC 8 μm and MIPS 24 μm images from Spitzer. The red plus sign in each panel marks the position of the pulsar PSR J0537−6910.

faint X-ray halo is detected at least 0.′5 farther out from the east shell rim. The X-ray shell and halo are better seen in Figure 3. In the top left panel of the X-ray image with contours, the X-ray shell is delineated by the lowest contour on the west side and the second-lowest contour on the east side, while the halo is delineated by the lowest contour on the east side. In the bottom right panel, the X-ray contours are plotted over the HST Hα image, clearly showing that the diffuse X-ray emission is much more extended than the Hα emission region.

The ASKAP 888 MHz map also peaks within the PWN. In addition, it shows an extended component. As the radio emission from 30 Dor B contains both a nonthermal (synchrotron radiation) component from the SNR and a thermal (bremsstrahlung radiation) component from the photo-ionized gas, we can compare the radio map to the X-ray and Hα images to assess the nature of the radio emission. The top right panel and bottom left panel of Figure 3 show radio contours over the radio image and over the X-ray image, respectively. The main part of the radio emission has many correspondences with the X-ray image: (1) both radio and X-ray images exhibit prominent emission from the PWN, (2) both exhibit a bright spot to the southeast of the PWN and appear to be bound by a long Hα arc in the HST image, and (3) the radio image shows a shell structure similar to the X-ray shell with similar surface brightness variations. The most obvious differences between the radio and X-ray images are the following: (1) radio emission is not detected in the faint X-ray halo region, and (2) the diffuse radio emission patches to the southeast and to the southwest of the main part have counterparts in the Hα but not X-rays. These southeast and southwest patches of radio emission and Hα emission most likely originate from diffuse photoionized gas, instead of shocked gas associated with the 30 Dor B SNR.

The Spitzer IRAC 8 μm image shows bright emission from the dark cloud in the south part of 30 Dor B, but no morphological feature can be unambiguously identified to be

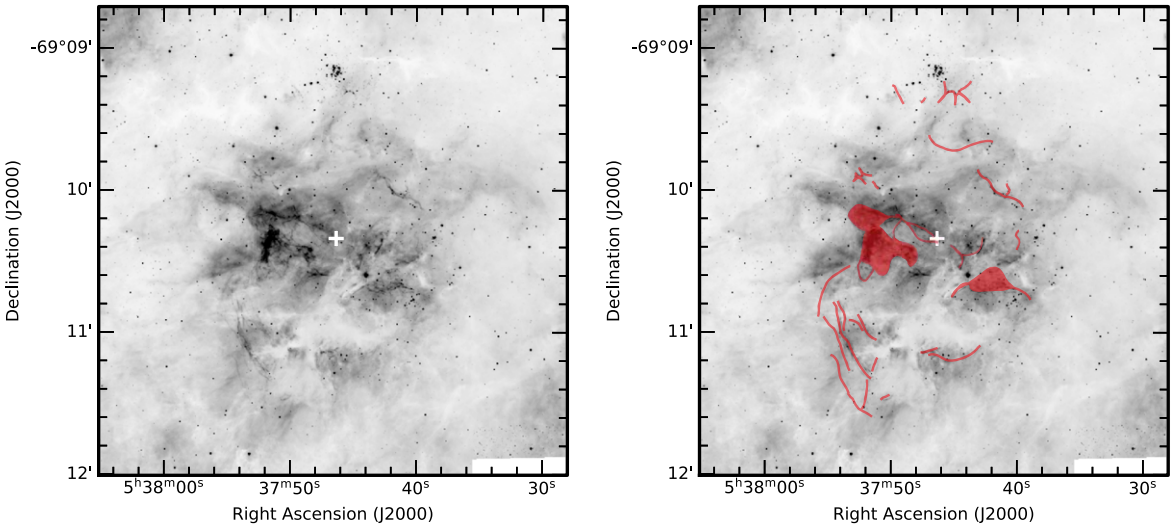

Figure 2. Left: close-up HST Hα image of 30 Dor B. Right: HST Hα image with sharp filaments marked. The white plus sign marks the position of the pulsar PSR J0537−6910.

associated with SNR shocks. The Spitzer MIPS 24 μm image shows a bright point source in the dark cloud and bright diffuse thermal dust emission, but no features are clearly associated with SNR shocks. The bright IR point source, 2MASS J05375027−6911071 or MSX LMC888, has been observed with the Spitzer IRS, and its spectrum shows nebular emission lines superposed on dust continuum emission, suggesting the presence of a compact H II region ionized by a young massive star (Micelotta et al. 2009), consistent with the young stellar object classification by Gruendl & Chu (2009).

4. Kinematic Detection of Shocks in 30 Dor B

The kinematic properties of the 30 Dor B region have been studied with long-slit high-dispersion echelle spectroscopic observations (Chu et al. 1992). The spectra were compared with those of H II regions, SNRs, superbubbles, and the 30 Dor giant H II region. They concluded that the 30 Dor B SNR was 1.′5 × 1.′2 in size and that high-velocity interstellar features were present to the north and to the east of the SNR. Given the extended diffuse X-ray emission revealed by the deep Chandra observation, we ought to reexamine the velocity structures, assess their relationship with the diffuse X-rays, and investigate whether these features are associated with a single SNR or multiple SNRs in 30 Dor B.

For easier visualization of correlations between the kinematic features and the morphological features, we mark the slit positions on the HST Hα image and the Chandra X-ray image and re-present the long-slit echellograms from Chu et al. (1992) with spatial extent and scale matching the slit positions marked in the images. The echellograms are displayed in two intensity scales, accentuating the bright low-velocity ISM in Figure 4 and the faint high-velocity material in Figure 5. The radial velocities are expressed in heliocentric velocities throughout this paper.

The bulk ionized gas in 30 Dor B is best seen in slit positions 1–3. The dense unperturbed photoionized gas in 30 Dor B has a constant radial velocity at 272 ± 5 km s^{-1}. To the south, slit positions 6 and 7 show that the bulk gas has a similar constant radial velocity. This constant velocity is most likely the systemic velocity of the general ISM in 30 Dor B. In slit positions 1–5, to the east of 30 Dor B the velocity profiles become broader and the central velocity shows significant variations, indicating a more perturbed velocity structure. In slit positions 8–10, the bright ionized gas in 30 Dor B shows a consistent constant radial velocity of ∼272 km s^{-1}, but the faint exterior to the north appears much more perturbed. Examples of narrow velocity profiles from quiescent regions (positions 2–W and 9–S marked in Figure 4) and broad velocity profiles from perturbed regions (positions 2–E and 9–N marked in Figure 4) are shown in Figure 6.

It has been observed in the LMC that confirmed SNRs show shell expansion velocities over 100 km $^{-1}$ or shocked material at >100 km s^{-1} velocity offsets, while photoionized H II regions are quiescent without any material accelerated to >100 km s^{-1} (Chu & Kennicutt 1988, 1994a). Thus, in Figures 4 and 5 we plot a thick dashed line at the bulk ISM velocity of 272 km s^{-1} and two auxiliary thin dashed lines at ±100 km s^{-1} offsets, respectively, to visualize interstellar features with velocity offsets greater than 100 km s^{-1} that are most certainly associated with SNRs.

Two types of high-velocity features are seen in the long-slit echellograms. The first type appears to be emanating from the quiescent interstellar velocity and extending to velocity offsets of 100–200 km s^{-1}; some of them curve back to the interstellar velocity, forming loop-like structures in the echellograms, while others end at highest velocity offsets, forming spikes or arc-like structures in the echellograms. Examples of these features are marked by magenta arrows in Figures 4 and 5. The second type appears as discrete high-velocity cloudlets without any connection to the quiescent interstellar velocity. Examples of these features are marked by cyan arrows in Figures 4 and 5. Based on these different types of features, Chu et al. (1992) argued that the first type of features was frequently seen in SNRs, and thus they must be associated with the 30 Dor B SNR, but they were uncertain about the second type of features and suggested that they were high-velocity interstellar clouds.

It can be seen in Figures 4 and 5 that these two types of high-velocity features are apparently associated with different interstellar environments. The first type is superposed on the brightest parts of the photoionized ISM in 30 Dor B, while the second type is observed outside the brightest parts of 30 Dor B. The surface brightness of the photoionized gas is proportional to the electron density squared; thus, a high surface brightness means a high gas density. Therefore, the first type of high-

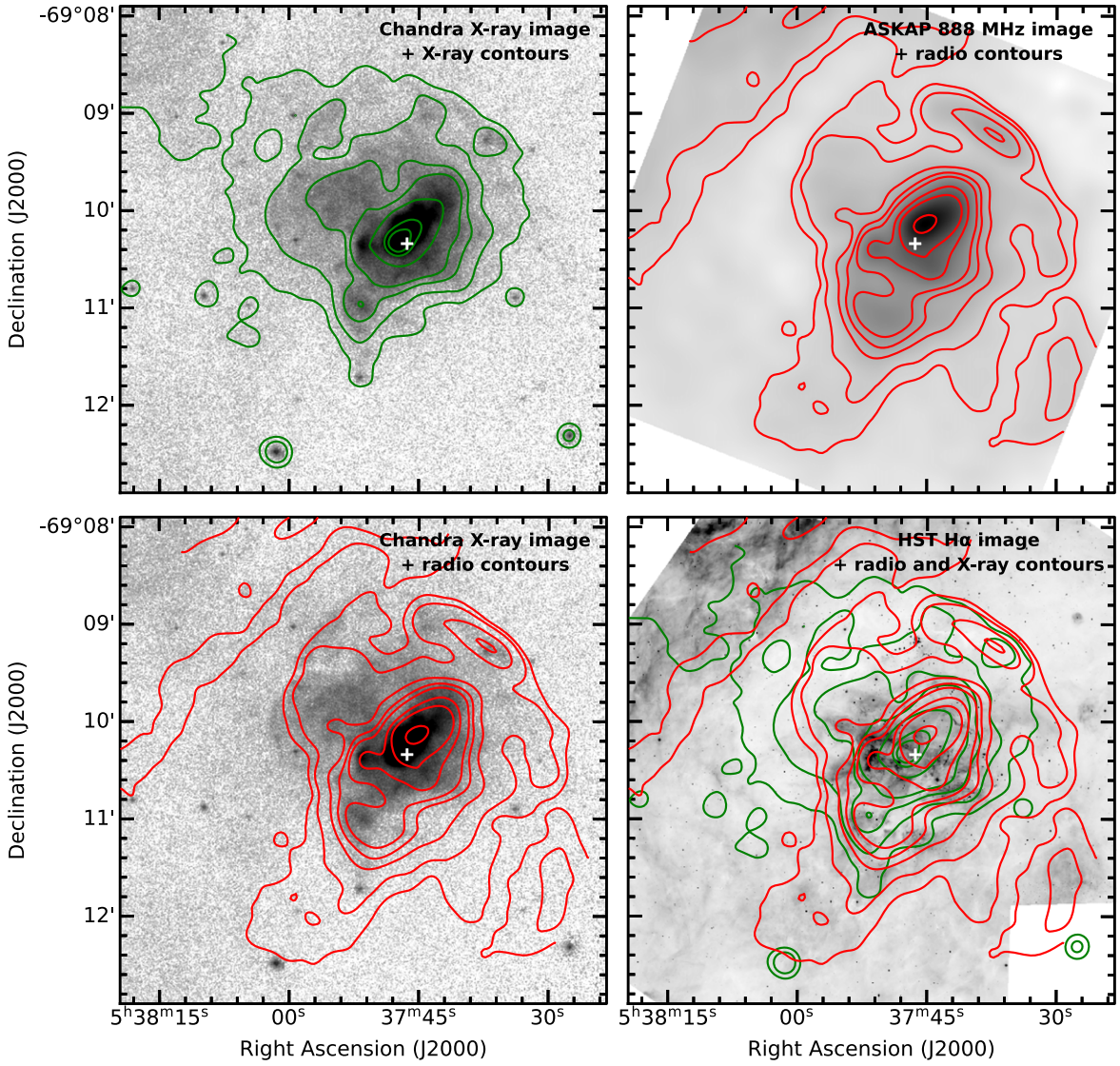

Figure 3. Top left: Chandra X-ray image in the 0.5–7.0 keV band shown in logarithm scale. The contour levels are 2.3×10^{-9}, 3.7×10^{-9}, 8.0×10^{-9}, 1.4×10^{-8}, 5.0×10^{-8}, 5.0×10^{-7}, and 1.0×10^{-6} counts s^{-1} cm^{-2}, extracted from the X-ray image smoothed by a Gaussian filter with $\sigma = 4''$. Top right: ASKAP 888 MHz image shown in square root scale. The contour levels are 0.007, 0.01, 0.02, 0.03, 0.04, 0.07, 0.1, and 0.2 Jy $beam^{-1}$. Bottom left: Chandra X-ray image overplotted with the radio contours from the top right panel. Bottom right: HST Hα image overplotted with the X-ray contours (green) from the top left panel and radio contours (red) from the top right panel. The white plus sign marks the position of the pulsar PSR J0537−6910.

velocity features is associated with shocks in an extended dense medium, while the second type of high-velocity feature is associated with discrete cloudlets in a tenuous medium.

Examining the locations of the high-velocity cloudlets and the distribution of diffuse X-ray emission in Figure 5, we can see that most of the high-velocity cloudlets are projected within the 2.′6-diameter X-ray shell. There are still some faint high-velocity cloudlets projected within the faint X-ray halo outside the X-ray shell, but these cloudlets have lower velocity offsets, generally <100 km s^{-1} from the quiescent interstellar velocity. Among these high-velocity cloudlets, only the brightest one in slit position 8 has an obvious counterpart in the HST Hα image, as shown in Figure 7. This 6″ high-velocity feature is resolved into knots strung along filaments. This morphology is seen in shocked interstellar cloudlets in core-collapse SNRs and in circumstellar medium in Type Ia SNRs (see examples given in Figure 8 of Li et al. 2021). Thus, these high-velocity features are most likely shocked and shredded cloudlets.

5. Discussion

The complex X-ray morphology and kinematic properties of 30 Dor B raise several questions: How effective are the SNR diagnostics at different wavelengths? Has 30 Dor B resulted from more than one SN explosion? Can the mass of the SN progenitor be assessed? The first question is addressed in Section 5.1 and the latter two in Section 5.2.

5.1. Effectiveness of SNR Diagnostics

Conventionally, SNRs are identified and confirmed by three signatures: diffuse X-ray emission, nonthermal radio emission, and high [S II]/Hα ratios. The multiwavelength views of 30 Dor B reveal that some diagnostics appear more effective than the others in a complex environment. The X-ray image is most effective in revealing shock-heated hot gas. It has been shown that XMM-Newton observations with ∼20 ks exposure can detect diffuse X-ray emission from an SNR in an ISM with densities as low as 0.01 H-atom cm^{-3} (Ou et al. 2018).

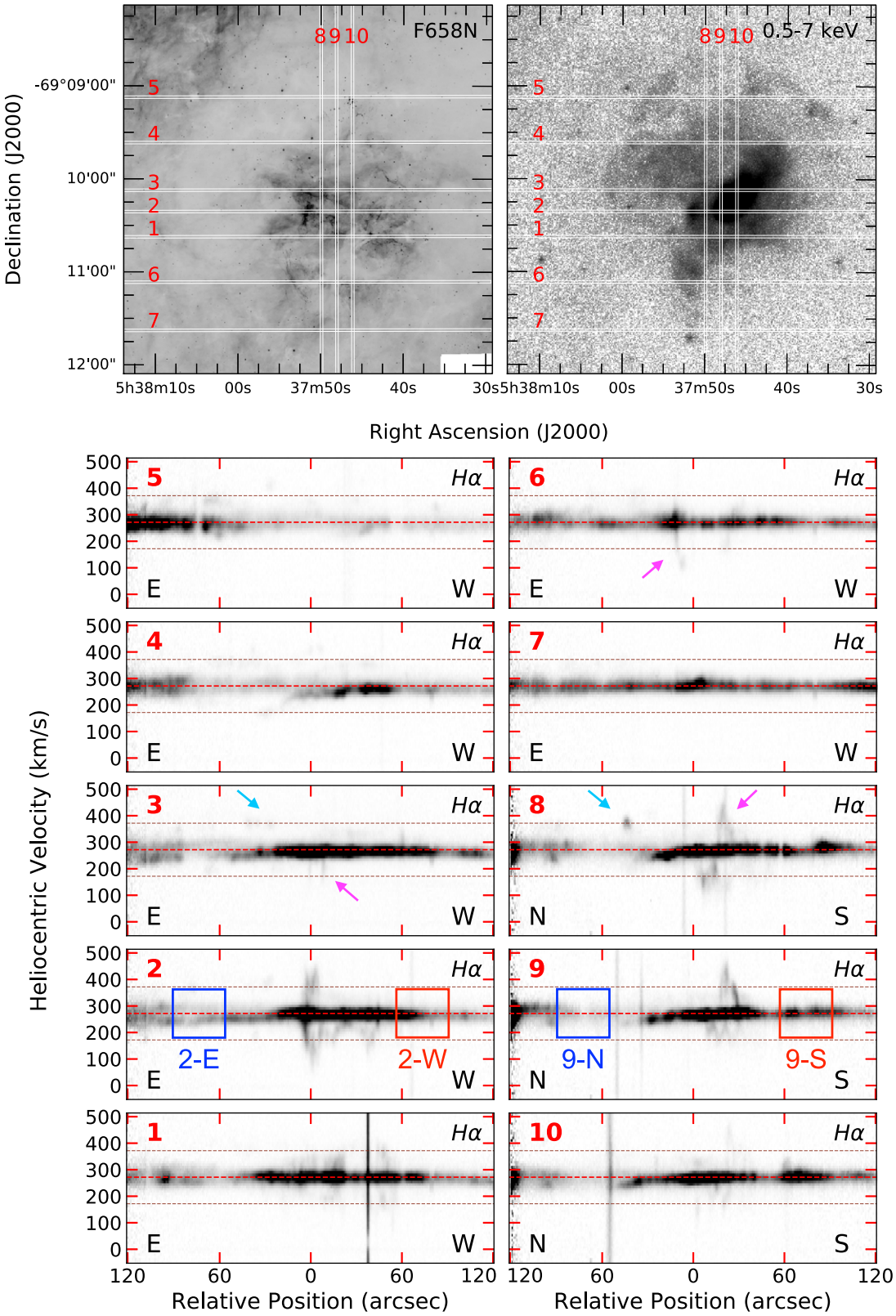

Figure 4. Top: CTIO echelle slit positions 1–10 overplotted on the HST F658N (left) and X-ray Chandra 0.5–7.0 keV (right) images. The X-ray image is displayed in logarithmic scale. Bottom: CTIO 4 m Hα echellograms displayed with spatial scale and extent matching the slit positions plotted in the top panels. The slit numbers are marked in the upper left corners in red. A thick dashed line is plotted at the bulk ISM velocity of 272 km s^{-1}, and two auxiliary thin dashed lines are plotted at $\pm$100 km s^{-1} offsets, respectively. Magenta arrows point at examples of high-velocity features emanating from the quiescent ISM velocity, and cyan arrows point at examples of discrete high-velocity cloudlets. Pixels affected by cosmic-ray hits have been fixed by interpolation between adjacent unaffected pixels. The Hα line profiles in boxes 2–E (blue), 2–W (red), 9–N (blue), and 9–S (red) are presented in Figure 6.

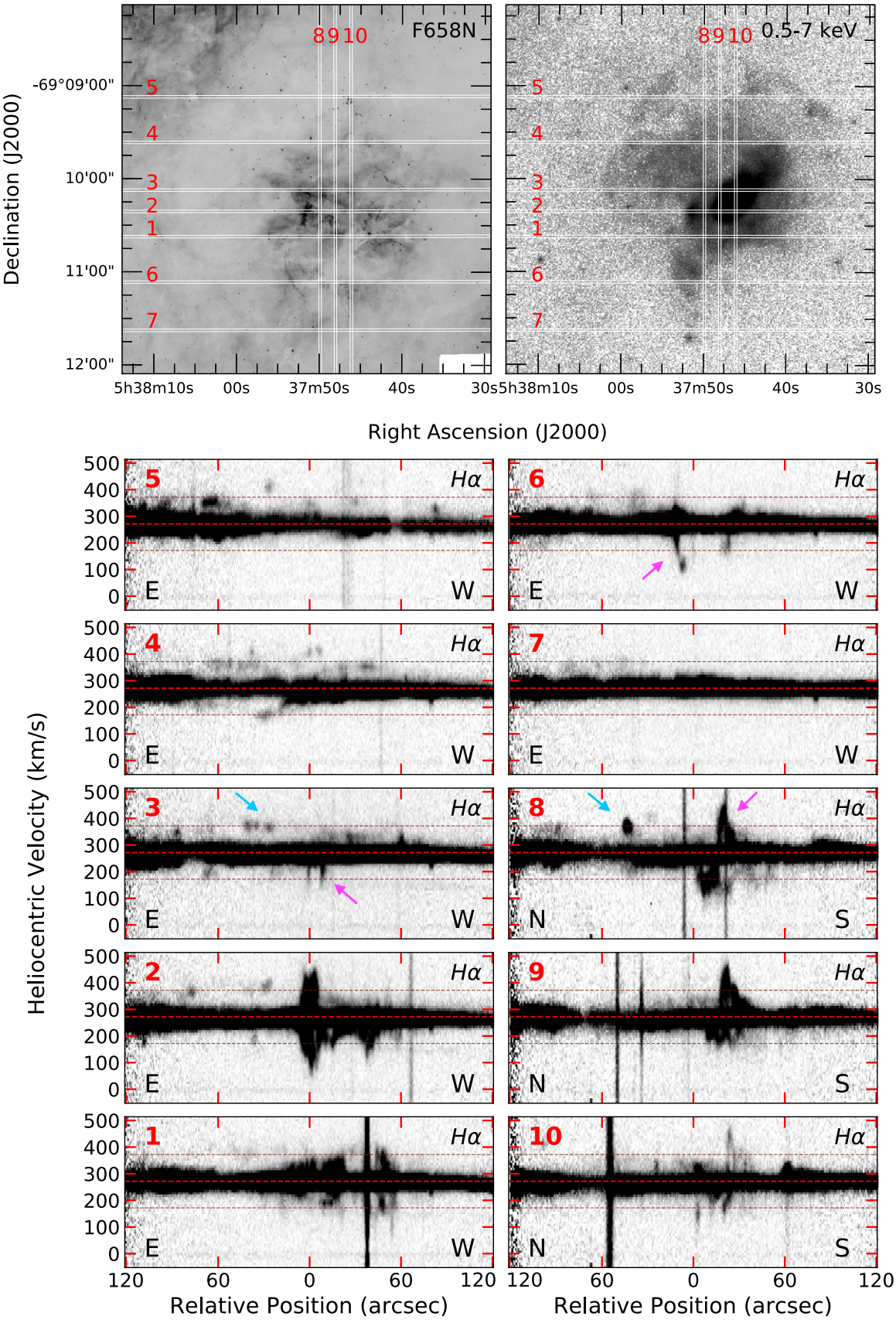

Figure 5. Same as Figure 4, but the echellograms in the bottom panels are displayed with a different intensity scale to accentuate the faint high-velocity features.

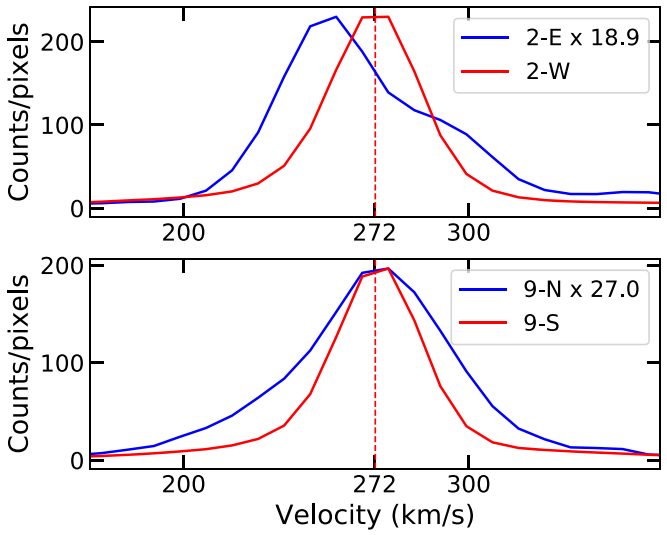

Figure 6. Top panel: Hα velocity profiles extracted from boxes 2–E (blue) and 2–W (red) along slit position 2. Bottom panel: Hα velocity profiles extracted from boxes 9–N (blue)and 9–S (red) along slit position 9. The box positions are marked in Figure 4. The fainter profile has been multiplied by a factor given in the upper right corner of the panel to match the peak of the brighter profile. The instrumental FWHM measured from the telluric lines is ~18 km s^{-1}; thus, even the narrow profiles are resolved.

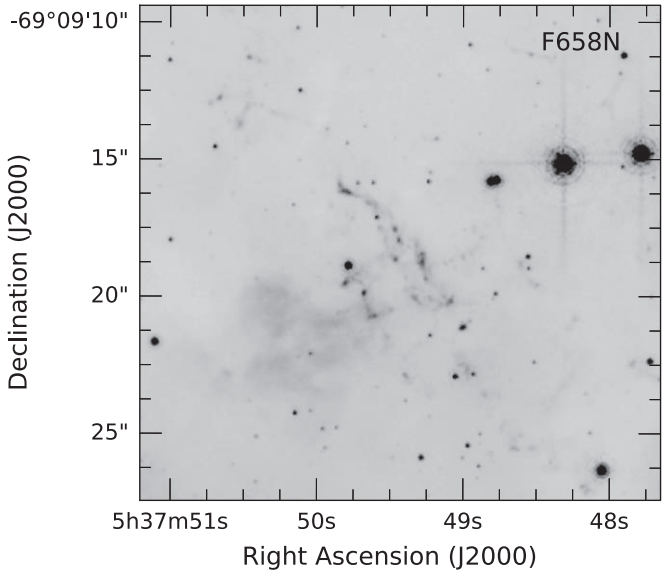

Figure 7. Close-up of shocked cloudlets.

Optical line emission from SNRs is more dependent on the physical conditions of the ambient medium. For a young Type Ia SNR in a partially neutral medium, its collisionless shocks produce hydrogen recombination lines, and its optical spectrum is dominated by Balmer lines (Chevalier et al. 1980; Heng 2010). For a young core-collapse SNR, if the SN progenitor was a massive O star and its strong stellar wind has already cleared out the ambient ISM, the SNR shock would advance in a low-density ionized medium and the post-shock material would be too hot and tenuous to emit detectable hydrogen Balmer lines; however, if remnant dense cloudlets remain in the surroundings of an SN progenitor, the SNR shocks into the dense cloudlets will become radiative early and emit optical lines and show high [S II]/Hα ratios, for example, the SNR N63A (Levenson et al. 1995). If an SN progenitor was an early B star without strong stellar wind, its dense ambient medium will cause the SNR shock to become radiative soon and produce bright line emission with high [S II]/Hα ratios, for example, the SNR N49 (Bilikova et al. 2007).

In the case of 30 Dor B, the SNR shocks advance into a complex ISM with both ionized gas and dusty neutral material. The colocation of the SNR and the ISM, as well as the similarity in their systemic velocities, suggests that the SNR is indeed interacting with the H II region in 30 Dor B. Because of the complex and nonuniform surrounding medium, no coherent SNR shell can form within the H II region, although fragmented partial shell structures are seen, as marked in Figure 2. On a larger scale, we see the X-ray shell that has no optical counterpart. This X-ray shell must be caused by the SNR shock advancing into an ionized low-density medium, and the shocks are not radiative yet. Thus, optical line images are not as effective as X-ray images in revealing SNR shocks.

Spectroscopic detection of shocked dense gas provides another useful diagnostic of SNR shocks. While the extended diffuse X-ray emission region does not show any optical shell counterpart, high-velocity cloudlets are detected in the Hα line. Similar high-velocity cloudlet features are commonly seen in 30 Dor; however, the photoionized H II region in 30 Dor is so bright that the faint high-velocity cloudlets cannot be identified morphologically in the Hα images (Chu & Kennicutt 1994b). In 30 Dor B, for the first time, a high-velocity cloudlet finds a morphological counterpart in an Hα image! As shown in Figure 7, the bright high-velocity cloudlet along slit position 8 is resolved in the HST Hα image into shreds of filaments and knots. The presence of high-velocity cloudlets in the diffuse X-ray emission region indicates that small dense cloudlets are embedded in a low-density ISM.

The [S II]/Hα ratio has been commonly used as a diagnostic in optical SNR surveys. SNRs in an isolated environment can have [S II]/Hα ratios approaching or greater than 1; however, SNRs superposed on H II regions will have this diagnostic diluted by the emission from the photoionized gas. Thus, a threshold of [S II]/Hα $\geqslant$ 0.45 has been used to identify extragalactic SNRs (e.g., Matonick & Fesen 1997). The [S II]/Hα ratio map of 30 Dor B (Figure 1) shows low values in the bright photoionized H II region and high values to the north of 30 Dor B. While there is some correspondence between the extended diffuse X-ray emission and the enhanced [S II]/Hα ratio, the details are confused by photoionization structures on the surface of dark clouds, large density variations, and complex stellar and interstellar environments, rendering the [S II]/Hα an ineffective SNR diagnostic in 30 Dor B.

[S II]/Hα ratio maps derived from the 4 m MOSAIC and the MCELS images are shown in Figure 8. The different appearances of these two maps amply illustrate the dilution of SNR emission by the background H II region emission. The MCELS images have a 2″ pixel size that is almost 10 times the width of the filaments resolved in the HST Hα image. The MOSAIC images have a higher resolution and a smaller pixel size, 0.″27; thus, the MOSAIC [S II]/Hα ratio map shows higher values and more fine structures. The [S II]/Hα ratio appears enhanced along an arc from the north to the east roughly along the rim of the X-ray shell and halo. As this arc is also just outside the photoionized gas, it is not clear whether the enhanced [S II]/Hα is caused by shocks or ionization fronts.

The comparisons among Hα, radio 888 MHz, and X-ray images described in Section 3 indicate that 888 MHz radio

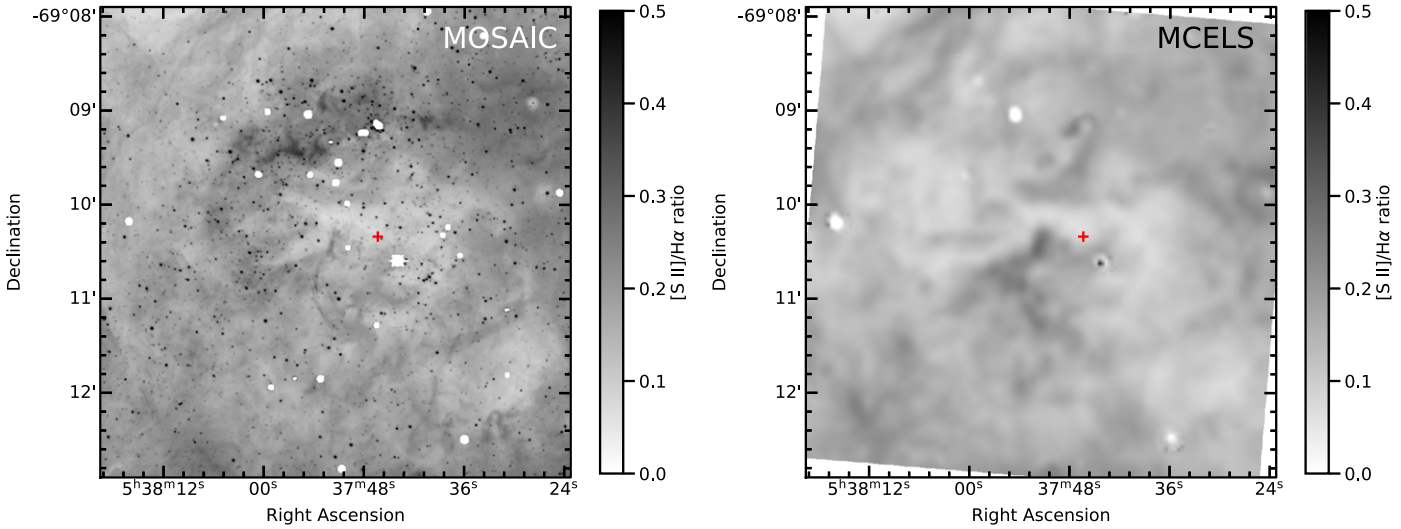

Figure 8. [S II]/Hα ratio maps derived from the 4 m MOSAIC images (left) and MCELS images (right). The white spots in the MOSAIC map are caused by saturated star images. The red plus sign marks the position of the pulsar.

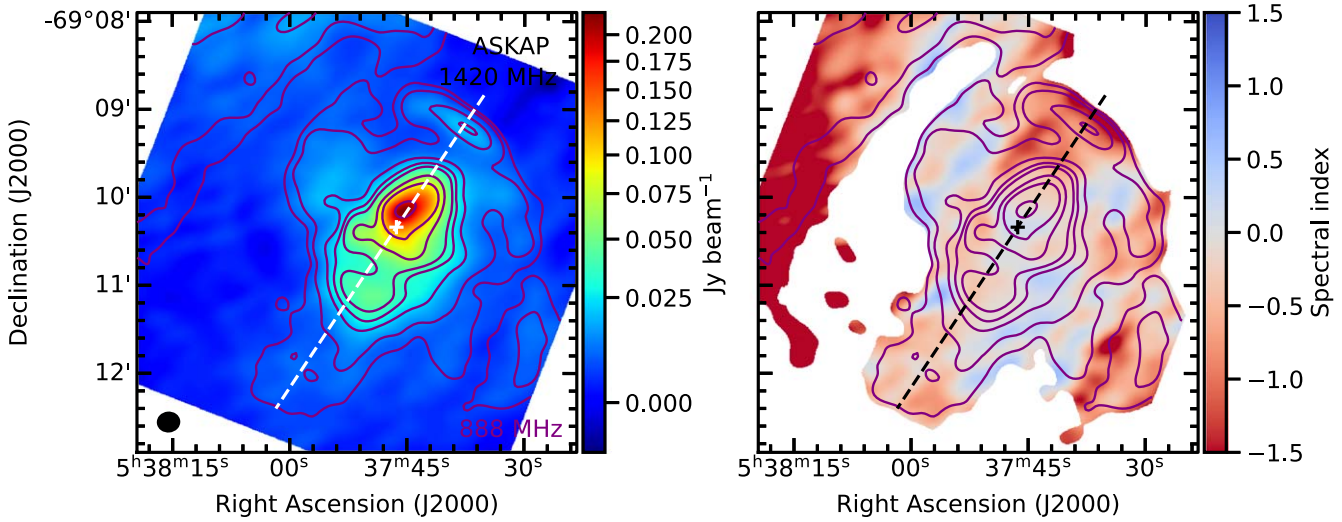

Figure 9. Left panel: ASKAP 1420 MHz map smoothed to match the angular resolution of the 888 MHz map. Right panel: spectral index map. Both panels are overplotted with contours from the 888 MHz map shown in Figure 3. In the spectral index map, only the regions with 888 MHz flux density $>15\sigma$ are shown, where $\sigma \sim 4 \times 10^{-4}$ Jy beam^{-1}. The plus sign marks the position of the pulsar. The dashed lines connect the radio/X-ray arc, PWN, pulsar, and the bright patches of emission inside and outside the X-ray-emitting regions. The very steep negative spectral index near the east edge of the map is part of the 30 Dor giant H II region.

maps can be as effective as X-ray images in detecting SNRs in an ionized low-density medium, where optical Hα emission cannot be detected. When multifrequency radio observations are available, the spectral index α in $S_\nu \propto \nu^\alpha$, where S_ν is the flux density and ν the frequency, can be derived to assess whether the radio emission is thermal or nonthermal. Normally, thermal emission has $\alpha \sim -0.1$ for an optically thin case and approaches 2 for an optically thick case, while α has a steep negative value for nonthermal emission. However, 30 Dor B is complicated by the superposing thermal emission from the photoionized H II region and the flat spectral index of the synchrotron radiation from its PWN. Figure 9 shows the 1420 MHz map convolved to match the resolution of the 888 MHz map and a spectral index map derived from these two maps of 30 Dor B. As the two frequencies are very close and the spectral index from the faint regions can be quite uncertain, we choose to present spectral index only within regions that are brighter than the lowest contour that delineates the SNR. This lowest contour corresponds to $\sim 18\sigma$ detection at 888 MHz. In the spectral index map, the radio-brightest region is associated with the PWN and shows a rather flat spectral index, fluctuating between $\sim$0.2 and ~ -0.2. This is consistent with the previous measurement of -0.19 determined from 3.5 and 6 cm observations (Lazendic et al. 2000). This radio-bright region is superposed on a bright H II region with very nonuniform surface brightness, which complicates the interpretation of the spectral index variations in the radio-brightest central region of 30 Dor B. It is impossible to disentangle the synchrotron radiation from the thermal emission, unless the radio maps are available over a larger range of frequencies with $\sim 1''$ resolution that matches the ground-based Hα image resolution.

Steep negative spectral indexes, <-1, are observed in the X-ray shell, particularly along the northwest rim, where a bright radio arc is present and coincides with an X-ray arc. It is interesting to note that the elongated radio emission in 30 Dor B and its vicinity seems to align with the pulsar and the elongated outflow of the pulsar wind. To the northwest end is the center of the radio/X-ray arc, while to the southeast exist a

bright radio/X-ray spot bordered by a sharp Hα arc in the HST image and a purely radio extension outside the SNR with spectral indexes ~ -0.5. The alignment of these features is illustrated by the dashed line drawn in each panel of Figure 9. It is tempting to suggest that these features may be associated with an outflow or a jet from the pulsar region. Nevertheless, it should be pointed out that outside the X-ray region there are two patches of radio emission, the aforementioned southeast extension and a detached southwest patch, and both have amorphous diffuse Hα emission counterparts. The nature of these two patches of radio/Hα emission is uncertain. Future radio observations with wider frequency coverage and higher angular resolution may help determine the nature of these features more accurately.

5.2. SN Progenitors of 30 Dor B

30 Dor B can be divided into three zones according to the distribution of X-ray emission and kinematic properties of the dense ionized gas. The innermost zone, ∼20 pc (1.′3) in size, shows SNR shocks impacting on the dense ionized gas in the bright H II region, in addition to the PWN. Incidentally, the region corresponds to the 1.′5 × 1.′2 SNR boundary suggested by Chu et al. (1992). The second zone is the X-ray shell that is about 40 pc (2.′6) across and extends much beyond the bright H II region, where high-velocity cloudlets with velocity offsets greater than 100 km s^{-1} are observed. The third zone is the faint X-ray halo exterior to the X-ray shell, where high-velocity cloudlets are observed but the velocity offsets are generally much less than 100 km s^{-1}. The distinct properties of these three zones are usually associated with SNRs at different evolutionary stages and/or interstellar environments. It is unlikely that one single SN is responsible for all these observed properties.

To examine the underlying stellar population in and around 30 Dor B, we have used the Magellanic Cloud Photometric Survey (MCPS; Zaritsky et al. 2004) to produce color–magnitude diagrams (CMDs) overplotted with stellar evolutionary tracks or isochrones, similar to the analysis of SNR B0532−67.5 (Li et al. 2022). The distributions of stars in the CMDs do not indicate a simple single burst of star formation; furthermore, there exist very massive stars whose masses cannot be determined reliably from photometry at optical wavelengths. Thus, we resort to the spectroscopic VLT-FLAMES Tarantula Survey (VFTS; Evans et al. 2011).

The VFTS has been used to make spectroscopic classifications of massive stars, assess their masses and ages, and determine the star formation history in NGC 2070 (aka 30 Dor) and NGC 2060 (aka 30 Dor B or LH99) by Schneider et al. (2018). They report that star formation in the past 8–10 Myr proceeded from north to northwest of 30 Dor toward southeast, along the molecular ridge between 30 Dor and 30 Dor B, and that the age distribution of the stars in 30 Dor B peaks at 4.4 Myr with a median of 5.7 Myr. They find that to the north of LH99, at $5^{h}37^{m}46^{s}$, $-69°09'10''$ (J2000), is the small association TLD 1, which is possibly 3.3–3.5 Myr old. Therefore, the star formation in 30 Dor B is by no means single-burst, and it is thus impossible to associate the SN progenitor with a particular stellar age group.

To illustrate the complexity of the stellar population in 30 Dor B, we have marked the spectral types of massive stars in Figure 10. Close-ups of TLD 1 and another crowded region are presented in Figure 11. It is evident that LH99 in 30 Dor B contains O2.5 to O3 main-sequence stars whose initial masses are greater than 100 $M_{\odot}$. The upper mass limit for massive stars to end in neutron stars is 25–30 $M_{\odot}$ (Heger et al. 2003). Thus, the progenitor of the pulsar in 30 Dor B could not have formed at the same time as these very massive stars, and no useful constraint on the SN progenitor's mass can be derived.

While we cannot assess the SN progenitor mass, we may assess whether the three zones with distinct X-ray and kinematic properties resulted from three different events. The central region of 30 Dor B associated with bright X-ray emission (including the PWN) and shocked ISM at velocity offsets greater than 200 km s^{-1} is likely the most recent SN event from a progenitor that had been a late O main-sequence star. The age of this SNR can be approximated by the spin-down time of its pulsar, 5000 yr (Marshall et al. 1998). If this SN event has also produced the X-ray shell, the expected expansion velocity of the X-ray shell, approximated by 0.5(radius/age), would be 4000 km s^{-1}. Such a high velocity would produce post-shock plasma at keV temperatures, which is not supported by the electron temperature of $kT \sim 0.3$ keV derived from modeling of the X-ray spectra (S. Ueda et al. 2023, in preparation). Therefore, this X-ray shell cannot be formed by the same SN event as the pulsar, and it must have resulted from an earlier SN explosion. The faint X-ray halo is much larger, and the shocked cloudlets have even smaller velocity offsets from the ISM; these properties are similar to those seen in large-scale diffuse X-ray emission whose SNRs can no longer be unambiguously identified or traced. Considering that star formation has been ongoing for the past several megayears, it is not surprising that multiple SNe have occurred within the vicinity of 30 Dor B. We conclude that the observed physical properties of 30 Dor B need at least two SN events. The faint X-ray halo may belong to a large-scale background produced by previous SN events.

6. Summary

30 Dor B, also cataloged as NGC 2060, is located at the southwest of the giant H II region 30 Dor. 30 Dor B contains the OB association LH 99, the H II region photoionized by LH 99, and MCSNR J0537−6910. The H II region is superposed by dark clouds, making it very difficult to study the boundary and structure of the SNR. Recent HST Hα images from the HTTP program (PI: E. Sabbi) have resolved the narrow filaments associated with SNR shocks, but no shell structure is observed. The deep 2 Ms Chandra X-ray image from the T-Rex program (PI: L. Townsley) has detected not only the PWN but also an extended X-ray shell ∼40 pc in size and an additional faint halo. The X-ray shell and halo are much more extended than the H II region of 30 Dor B. The ASKAP 888 MHz map of 30 Dor B shows counterparts to all X-ray emission features except the faint X-ray halo.

We have reanalyzed the high-dispersion long-slit echelle observations of Chu et al. (1992). In addition to the quiescent component of unperturbed ISM at 272 ± 5 km s^{-1}, we find two types of high-velocity features offset by more than 100 km s^{-1}. The first type appears to emanate from the quiescent interstellar velocity and extend to velocity offsets of 100–200 km s^{-1}, and these features are associated with dense ISM. In contrast, the second type appears as discrete high-velocity cloudlets without any connection to the quiescent interstellar velocity, and these features are associated with less dense ISM. We further find that high-velocity features of the first type are associated with the central X-ray-bright region, while those of the second type are within the extended X-ray shell. There are high-velocity cloudlets within the

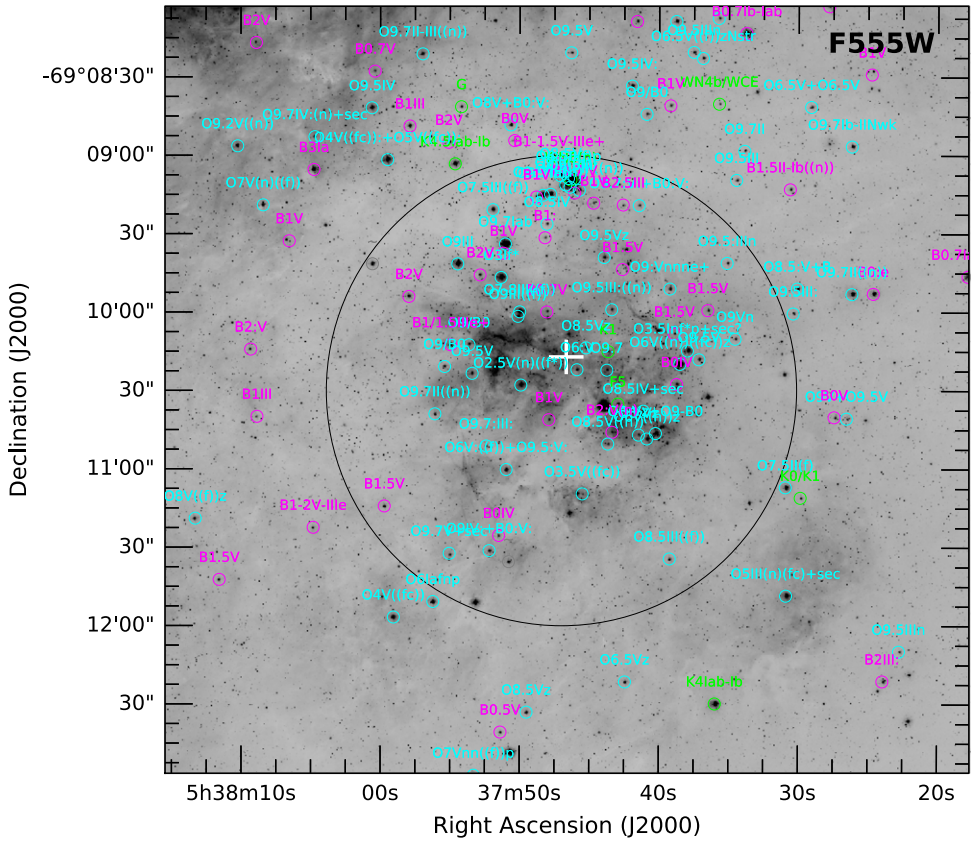

Figure 10. The HST F555W image of the SNR 30 Dor B and its environment. The spectral types of massive stars from the VLT-FLAMES Tarantula Survey (Evans et al. 2011) are marked, with O and B stars in cyan and magenta, respectively. Late-type supergiants and Wolf-Rayet stars are marked in green. The 16 ms pulsar in the SNR is marked with a white plus sign. The 3′-diameter circle marks a rough boundary of the OB association LH99 (Lucke & Hodge 1970).

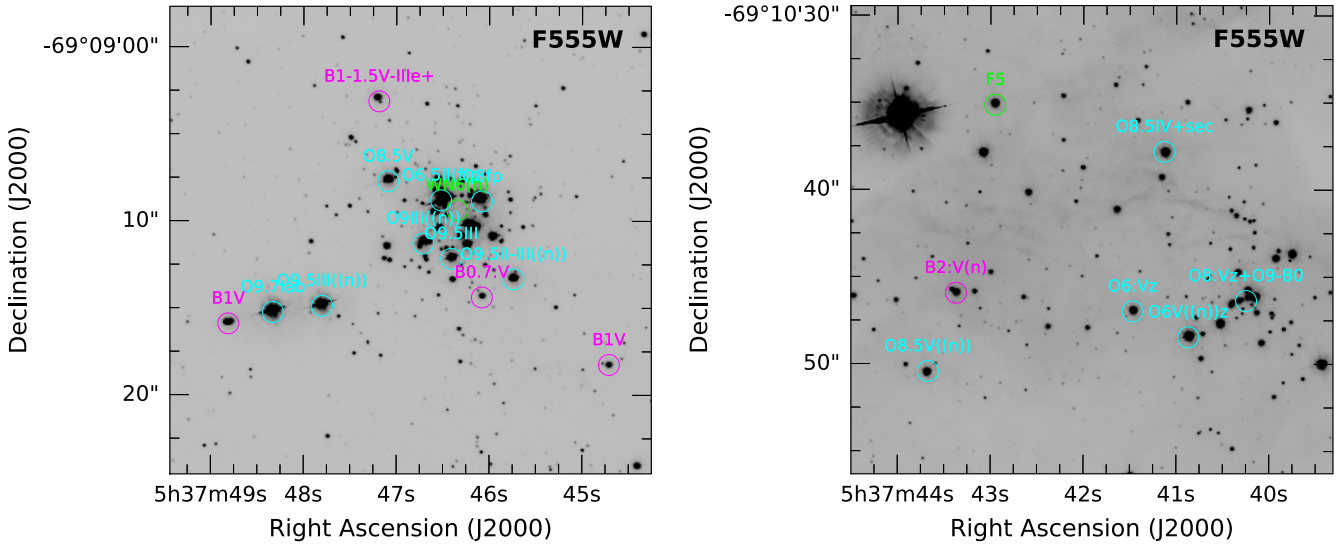

Figure 11. Close-up images for two crowded regions in Figure 10. The small cluster in the left panel is TLD 1.

faint X-ray halo, but their velocity offsets from the quiescent interstellar velocity are usually <100 km s^{-1}.

The multiwavelength observations of 30 Dor B are used to evaluate the effectiveness of the three common SNR diagnostics: diffuse X-ray emission, [S II]/Hα ratio, and nonthermal radio spectral index. In 30 Dor B's complex environment, where an SNR is superposed on a photoionized H II region dissected by dark clouds, diffuse X-ray emission offers the most effective diagnostic of SNRs, while the [S II]/Hα ratio is the least effective diagnostic of SNR shocks. Radio emission is more effective than optical emission in detecting SNRs, but the confusion caused by the superposed thermal emission renders the spectral index less effective in diagnosing SNR accurately.

The spectroscopic VFTS survey of massive stars in 30 Dor B is used to deduce that star formation has been going on for the past 8–10 Myr and that the most massive stars in 30 Dor B have initial masses greater than 100 $M_{\odot}$ (Schneider et al. 2018). Based on this information, we conclude that the SN progenitor mass cannot be

assessed from the complex star formation history and stellar population. Adopting the pulsar's spin-down time of 5000 yr as the SNR age, the X-ray shell would have to be expanding at 4000 km s^{-1} to be produced by the same SN explosion. Such a fast expansion would produce post-shock plasma temperature incompatible with that indicated by X-ray spectra. We conclude that at least two SN events had occurred in 30 Dor B and that the faint X-ray halo may require additional previous SN events.

Acknowledgments

We thank the anonymous referee for prompt reviews and constructive suggestions to improve this paper. We also thank Dr. John Raymond for useful discussions on shocks. Y.-H.C. and C.-J.L. acknowledge the support of the NSTC grants 110-2112-M-001-020 and 111-2112-M-001-063, and S.U. acknowledges the NSTC grant NSTC 111-2112-M-001-026-MY3 from the National Science and Technology Council of Taiwan.

This research has made use of NASA's Astrophysics Data System Bibliographic Services and the SIMBAD database, operated at CDS, Strasbourg, France (Wenger et al. 2000). This paper has used data obtained from the Chandra Data Archive and the Chandra Source Catalog and software provided by the Chandra X-ray Center (CXC) in the application packages CIAO and Sherpa. This paper has also used observations at Cerro Tololo Inter-American Observatory at NSF's NOIRLab, which is managed by the Association of Universities for Research in Astronomy (AURA) under a cooperative agreement with the National Science Foundation. Also used in this paper are ASKAP 888 and 1420 MHz maps. The Australian SKA Pathfinder (ASKAP) is part of the Australia Telescope National Facility, which is managed by CSIRO. Operation of ASKAP is funded by the Australian Government with support from the National Collaborative Research Infrastructure Strategy. ASKAP uses the resources of the Pawsey Supercomputing Centre. Establishment of ASKAP, the Murchison Radio-astronomy Observatory, and the Pawsey Supercomputing Centre are initiatives of the Australian Government, with support from the Government of Western Australia and the Science and Industry Endowment Fund. We acknowledge the Wajarri Yamatji people as the traditional owners of the Observatory site. This work is based in part on observations made with the Spitzer Space Telescope, which was operated by the Jet Propulsion Laboratory, California Institute of Technology under a contract with NASA.

Facilities: CXO (ACIS), HST (ACS, WFC3), Blanco, Spitzer (IRAC, MIPS), ASKAP.

Software: SAOImage DS9 (Joye & Mandel 2003), Astropy (Astropy Collaboration et al. 2013, 2018, 2022), Matplotlib (Hunter 2007), NumPy (van der Walt et al. 2011; Harris et al. 2020), SciPy (Virtanen et al. 2020), CIAO (Fruscione et al. 2006), XSPEC (Arnaud 1996).

ORCID iDs

Wei-An Chen (陳韋安) https://orcid.org/0000-0002-8336-2837
Chuan-Jui Li (李傳睿) https://orcid.org/0000-0003-1449-7284
You-Hua Chu (朱有花) https://orcid.org/0000-0003-3667-574X
Shutaro Ueda (上田周太朗) https://orcid.org/0000-0001-6252-7922
Kuo-Song Wang (王國松) https://orcid.org/0000-0002-9323-0950
Sheng-Yuan Liu (呂聖元) https://orcid.org/0000-0003-4603-7119
Bo-An Chen (陳柏安) https://orcid.org/0009-0002-1602-2282

References

Arnaud, K. A. 1996, adass V, 101, 17
Astropy Collaboration, Price-Whelan, A. M., Lim, P. L., et al. 2022, ApJ, 935, 167
Astropy Collaboration, Price-Whelan, A. M., Sipőcz, B. M., et al. 2018, AJ, 156, 123
Astropy Collaboration, Robitaille, T. P., Tollerud, E. J., et al. 2013, A&A, 558, A33
Bilikova, J., Williams, R. N. M., Chu, Y.-H., et al. 2007, AJ, 134, 2008
Chevalier, R. A., Kirshner, R. P., & Raymond, J. C. 1980, ApJ, 235, 186
Chu, Y.-H. 1997, AJ, 113, 1815
Chu, Y.-H., & Kennicutt, R. C. 1988, AJ, 95, 1111
Chu, Y.-H., & Kennicutt, R. C. 1994a, Ap&SS, 216, 253
Chu, Y.-H., & Kennicutt, R. C. 1994b, ApJ, 425, 720
Chu, Y.-H., Kennicutt, R. C., Schommer, R. A., et al. 1992, AJ, 103, 1545
Evans, C. J., Taylor, W. D., Hénault-Brunet, V., et al. 2011, A&A, 530, A108
Fruscione, A., McDowell, J. C., Allen, G. E., et al. 2006, Proc. SPIE, 6270, 62701V
Garmire, G. P., Bautz, M. W., Ford, P. G., et al. 2003, Proc. SPIE, 4851, 28
Gruendl, R. A., & Chu, Y.-H. 2009, ApJS, 184, 172
Harris, C. R., Millman, K. J., van der Walt, S. J., et al. 2020, Natur, 585, 357
Heger, A., Fryer, C. L., Woosley, S. E., et al. 2003, ApJ, 591, 288
Heng, K. 2010, PASA, 27, 23
Henize, K. G. 1956, ApJS, 2, 315
HESS Collaboration, Abramowski, A., Acero, F., et al. 2012, MNRAS, 424, 128
Hunter, J. D. 2007, CSE, 9, 90
Joye, W. A., & Mandel, E. 2003, adass XII, 295, 489
Lazendic, J. S., Dickel, J. R., Haynes, R. F., et al. 2000, ApJ, 540, 808
Le Marne, A. E. 1968, MNRAS, 139, 461
Levenson, N. A., Kirshner, R. P., Blair, W. P., et al. 1995, AJ, 110, 739
Li, C.-J., Chu, Y.-H., Chuang, C.-Y., et al. 2022, AJ, 163, 30
Li, C.-J., Chu, Y.-H., Raymond, J. C., et al. 2021, ApJ, 923, 141
Long, K. S., Helfand, D. J., & Grabelsky, D. A. 1981, ApJ, 248, 925
Lucke, P. B., & Hodge, P. W. 1970, AJ, 75, 171
Marshall, F. E., Gotthelf, E. V., Zhang, W., et al. 1998, ApJL, 499, L179
Matonick, D. M., & Fesen, R. A. 1997, ApJS, 112, 49
Meixner, M., Gordon, K. D., Indebetouw, R., et al. 2006, AJ, 132, 2268
Micelotta, E. R., Brandl, B. R., & Israel, F. P. 2009, A&A, 500, 807
Mills, B. Y., Turtle, A. J., & Watkinson, A. 1978, MNRAS, 185, 263
Ou, P.-S., Chu, Y.-H., Maggi, P., et al. 2018, ApJ, 863, 137
Pennock, C. M., van Loon, J. T., Filipović, M. D., et al. 2021, MNRAS, 506, 3540
Sabbi, E. 2016, Hubble Tarantula Treasury Project: 30DOR (HTTP) (Baltimore, MD: STScI)
Sabbi, E., Anderson, J., Lennon, D. J., et al. 2013, AJ, 146, 53
Sabbi, E., Lennon, D. J., Anderson, J., et al. 2016, ApJS, 222, 11
Schneider, F. R. N., Ramírez-Agudelo, O. H., Tramper, F., et al. 2018, A&A, 618, A73
Smith, R. C. & MCELS Team 1999, in IAU Symp. 190, New Views of the Magellanic Clouds, ed. Y.-H. Chu et al. (San Francisco, CA: ASP), 28
van der Walt, S., Colbert, S. C., & Varoquaux, G. 2011, CSE, 13, 22
Virtanen, P., Gommers, R., Oliphant, T. E., et al. 2020, NatMe, 17, 261
Wang, Q. D., Gotthelf, E. V., Chu, Y.-H., et al. 2001, ApJ, 559, 275
Wenger, M., Ochsenbein, F., Egret, D., et al. 2000, A&AS, 143, 9
Zaritsky, D., Harris, J., Thompson, I. B., et al. 2004, AJ, 128, 1606